Data Descriptor

Experimental Spectroscopic Data of SnO$_2$ Films and Powder

Hawazin Alghamdi [1], Olasunbo Z. Farinre [1], Mathew L. Kelley [2,3], Adam J. Biacchi [2], Dipanjan Saha [2], Tehseen Adel [2], Kerry Siebein [2], Angela R. Hight Walker [2], Christina A. Hacker [2], Albert F. Rigosi [2] and Prabhakar Misra [1,*]

1 Department of Physics and Astronomy, Howard University, Washington, DC 20059, USA
2 Physical Measurement Laboratory, National Institute of Standards and Technology, Gaithersburg, MD 20899, USA
3 Theiss Research, La Jolla, CA 92037, USA
* Correspondence: pmisra@howard.edu

Abstract: Powders and films composed of tin dioxide (SnO$_2$) are promising candidates for a variety of high-impact applications, and despite the material's prevalence in such studies, it remains of high importance that commercially available materials meet the quality demands of the industries that these materials would most benefit. Imaging techniques, such as scanning electron microscopy (SEM), atomic force microscopy (AFM), were used in conjunction with Raman spectroscopy and X-ray photoelectron spectroscopy (XPS) to assess the quality of a variety of samples, such as powder and thin film on quartz with thicknesses of 41 nm, 78 nm, 97 nm, 373 nm, and 908 nm. In this study, the dependencies of the corresponding Raman, XPS, and SEM analysis results on properties of the samples, like the thickness and form (powder versus film) are determined. The outcomes achieved can be regarded as a guide for performing quality checks of such products, and as reference to evaluate commercially available samples.

Keywords: tin (IV) oxide powder; X-ray photoelectron spectroscopy; Raman spectroscopy

1. Summary

Tin (IV) oxide (SnO$_2$) has a large range of applications in today's world, and there are fields in which the use of SnO$_2$ has become incredibly important. Some of these efforts seek to develop and optimize environmental detectors [1–8], solar cell technologies [9–23], and solid-state chemical sensors [24–36]. This n-type semiconductor has been utilized in ancient civilizations in a variety of applications from ceramic dye to polishing and glass coatings [37]. SnO$_2$ has also been useful in the development of optical filters [38–40], photovoltaic devices [41–44], and materials dedicated to catalytic processes [45–50]. In addition to these applications, this material can also be used for lithium–ion batteries and photocatalysis [51,52].

These applications have led to the wide commercial availability of SnO$_2$. With this ease of sample acquisition, it also remains important for materials to be tested for quality and compared with other counterparts in the literature. Some of the ways in which one may assess the various properties of SnO$_2$ are through the measurement of its surface, optical, and electrical properties.

In this work, imaging techniques, such as scanning electron microscopy (SEM) and atomic force microscopy (AFM), were used in conjunction with Raman spectroscopy and X-ray photoelectron spectroscopy (XPS) to assess the quality of a variety of samples, many of which differ in thickness and were either prepared as films or powders. As such, the dependencies of the corresponding Raman spectra, XPS surveys, and SEM images on properties such as the thickness have been determined and reported here as a guide for those performing similar quality checks as well as to add to the statistics of reproducible results for commercially available samples.

2. Data Description

2.1. Scanning Electron and Atomic Force Microscopy

Scanning electron microscopy was used to gain an initial understanding on how the powder and film SnO_2 samples appeared in terms of grain sizes and uniformity. As such, these resulting images, shown in Figure 1 and whose parameter data are provided in the Methods section, show that the superficial layers within thicker samples (notably the 908 nm and 373 nm) are not as uniform. Such an appearance may result by way of thermal cracking or by spontaneous seeding (the samples were not annealed during the SEM process, only during manufacturing). This interpretation can be supported by the behavior where, at 373 nm, smaller clusters appear to form than in the case of the 908 nm film (Figure 2). The SEM images also reveal that, for the films thinner than 373 nm, the superficial surface layers appear more uniform. Given that the same measurement parameters were used for all samples, it appears that the 41 nm has the least disordered appearance from all of the films. As far as the powder samples are concerned, their clusters appear more unbounded, with almost a near-spherical smoothness, at least within the 100 nm measurement scale used for all images. Energy Dispersive Spectroscopy (EDS) analysis was carried out on the 908 nm thick sample to confirm the chemical elements of SnO_2 (Figure 3). The composition came out to be 31.3% Sn (by weight) and 68.7% O (by weight). The EDS data confirmed that the film is indeed SnO_2.
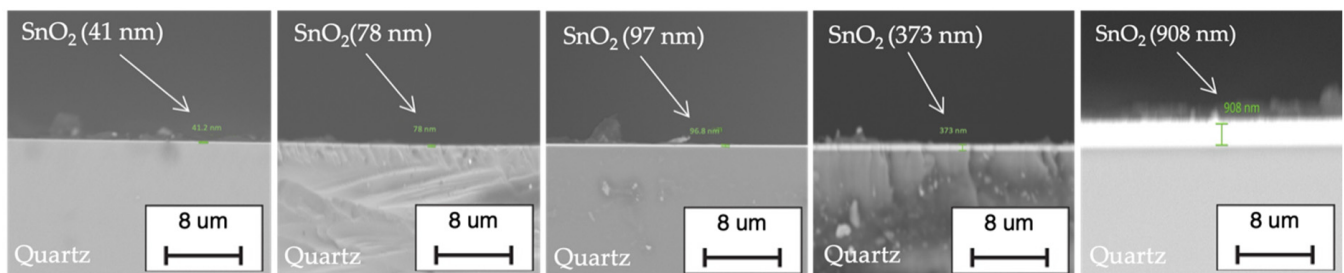
Figure 1. SEM images show cross-section images of SnO_2 films of six different thicknesses (i.e., 41 nm, 78 nm, 97 nm, 373 nm, and 908 nm.
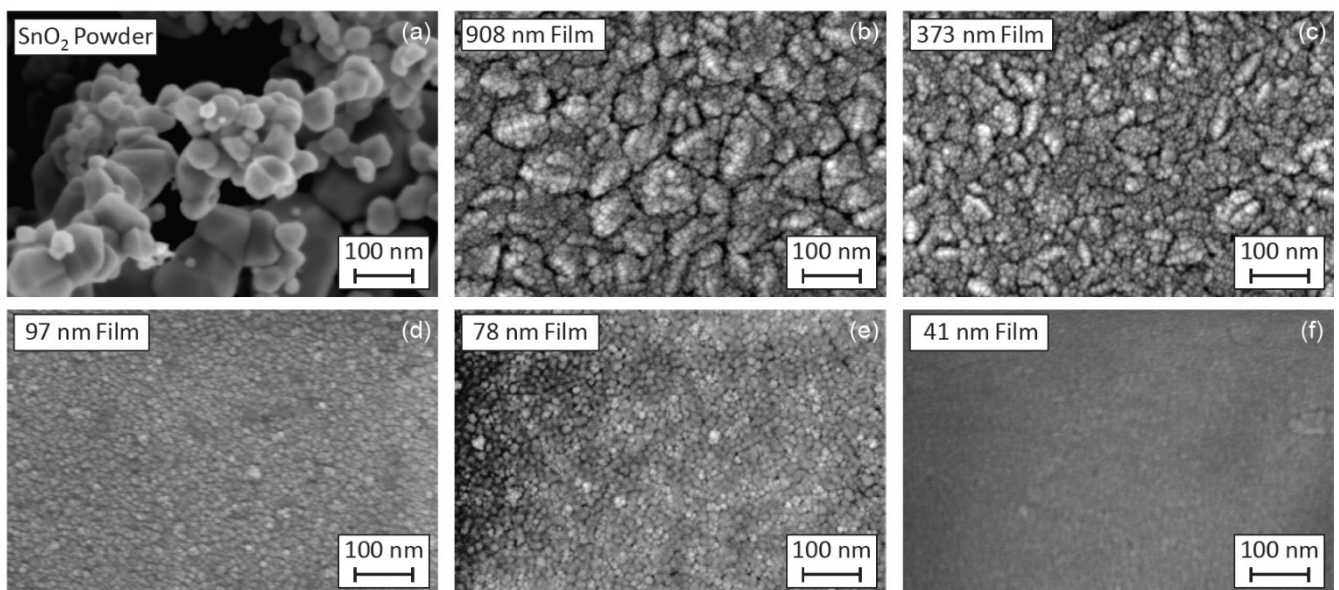

Figure 2. These SEM images show SnO_2 films of six different thicknesses or forms at similar magnifications: (**a**) powder, (**b**) 908 nm thick, (**c**) 373 nm thick, (**d**) 97 nm thick, (**e**) 78 nm thick, and (**f**) 41 nm thick. Relevant measurement parameters can be found in the Methods section.
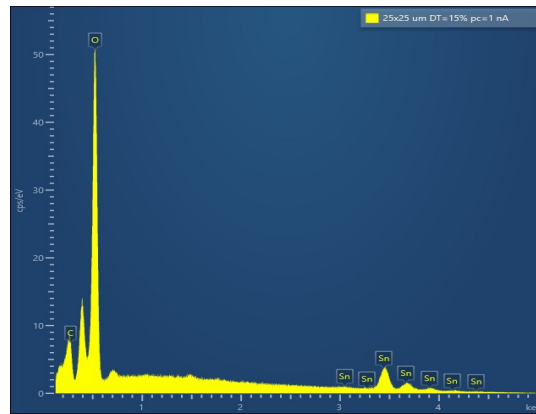
Figure 3. EDS analysis of 908 nm film thickness.

AFM images were acquired for the samples shown in Figure 4a,b (908 nm and 373 nm, respectively) to gain a better understanding of the expected surface roughness that results from the clustering seen superficially. From the two-dimensional profiles measured, the texture for the 908 nm film appeared more granular than its 373 nm counterpart, whose microscope grains appear slightly smoother. A three-dimensional roughness display was plotted and is displayed below the images in Figure 4 as a visualization of the difference in surface roughness between the two films. Though the difference in smoothness between the two films is more obvious in this three-dimensional picture, it is still beneficial to quantify that difference via the root-mean-square (RMS) roughness. This quantity may be calculated by software such as Gwyddion.[a] It was found that the RMS roughness for the 908 nm and 373 nm films was about 8.8 nm and 5.4 nm, respectively. It should be noted that these two thicknesses were the only ones measurable without error (that is, other images have sections indicative of AFM tip damage and error).
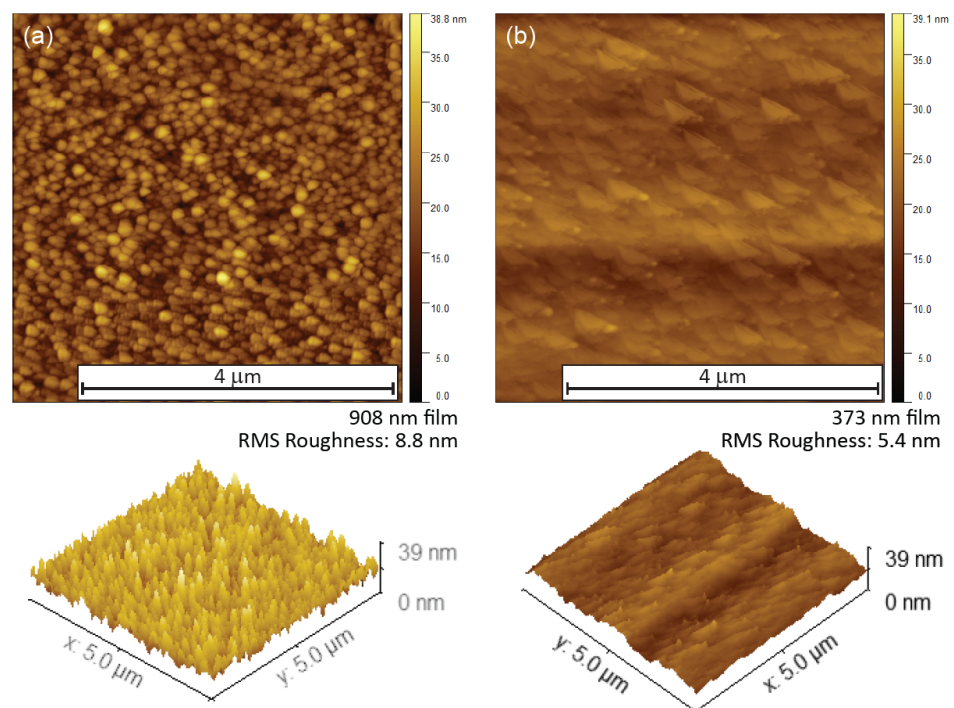
Figure 4. Comparative data are shown for two atomic force microscope (AFM) images obtained on a (**a**) 908 nm film and a (**b**) 373 nm film. A three-dimensional roughness display is shown below the images as a visualization of the difference in surface roughness between the two films. The scale on the roughness ranges from 0 nm to 39 nm, where the average thickness value is the center of the scale (18.5 nm). The variation generally falls within the ranges shown.

2.2. Raman Spectroscopy

Raman spectroscopy was utilized to gain a further understanding of these samples' optical properties. In the first set of tests, powder samples were compressed into pellets and then loaded into a cryogenic chamber with temperature control. The intent was to conduct thermal cycling starting from the highest temperature available on the measurement system (400 °C), and then repeat every set of data by starting from the lowest temperature available on the measurement system (−193 °C). In all cases, these data provided insight into which vibrational modes were present and whether or not these observations were consistent with what has been reported in earlier work. This optical check is one way by which industries can verify the quality of semiconductor materials. All experimental parameters are listed in the Methods section.

Figure 5 shows data from the powder samples. These data are temperature dependent and have endpoints of −193 °C and 400 °C resulting from the limits of the measurement system.[#] The corresponding data in Figure 5b for measurements performed with a reverse order of temperature steps, starting with the highest temperature, do not show any obvious hysteresis when compared with Figure 5a. This similarity and lack of hysteresis is best seen in Figure 6. For the datasets in Figure 6b–d, three vibrational modes are tracked, namely the E_g, A_{1g}, and B_{2g} modes, located at (for −193 °C) 476.6 cm^{-1}, 636.5 cm^{-1}, and 779.5 cm^{-1}, respectively. Figure 5a,b shows a subset of peaks (for visual clarity) whose centers align with the three dashed vertical lines. These demarcations have been aligned with the coldest temperature data to provide a visualization for the amount by which a given peak shifts with temperature. These shifts, along with the formal assignment of the modes, are provided in Figure 6.
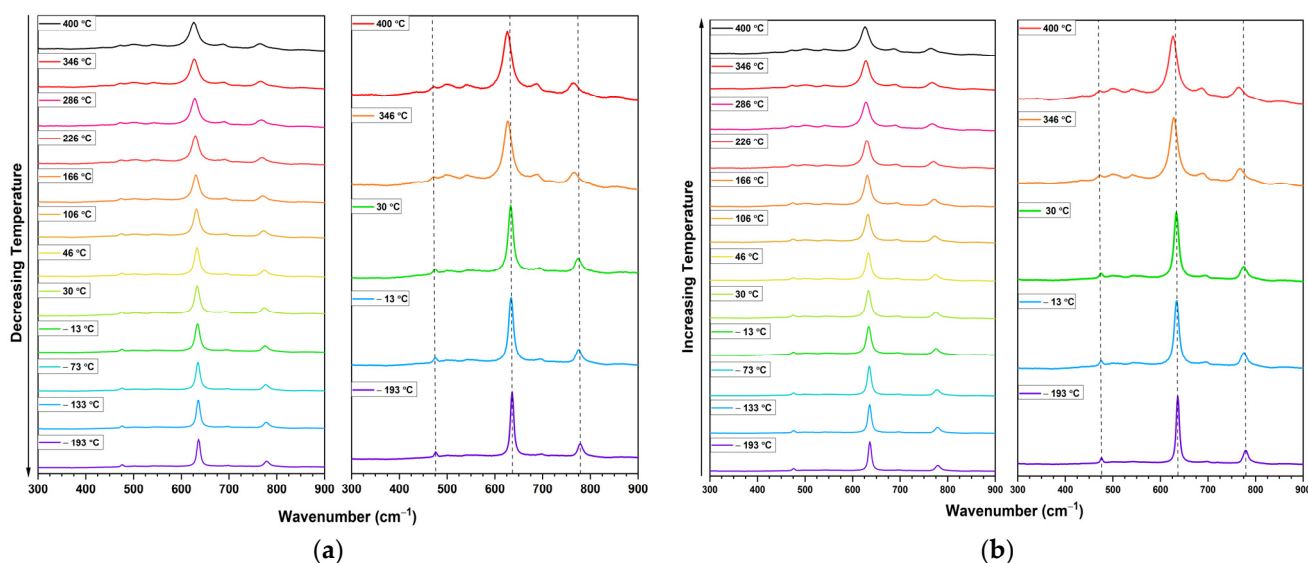
Figure 5. Powder samples were measured at experimental parameters listed in the Methods section. Powder was compressed into standard pellets prior to measurement and subsequently loaded into a cryogenic chamber with temperature control. (**a**) A series of Raman spectra are shown as a function of temperature, starting with −193 °C and ending at 400 °C with five spectra were plotted with greater vertical scaling to distinguish the changes apparent with some of the vibrational modes. (**b**) Measurements were generally repeated with temperatures decreasing from 400 °C to assess any hysteresis or other unaccounted effects.
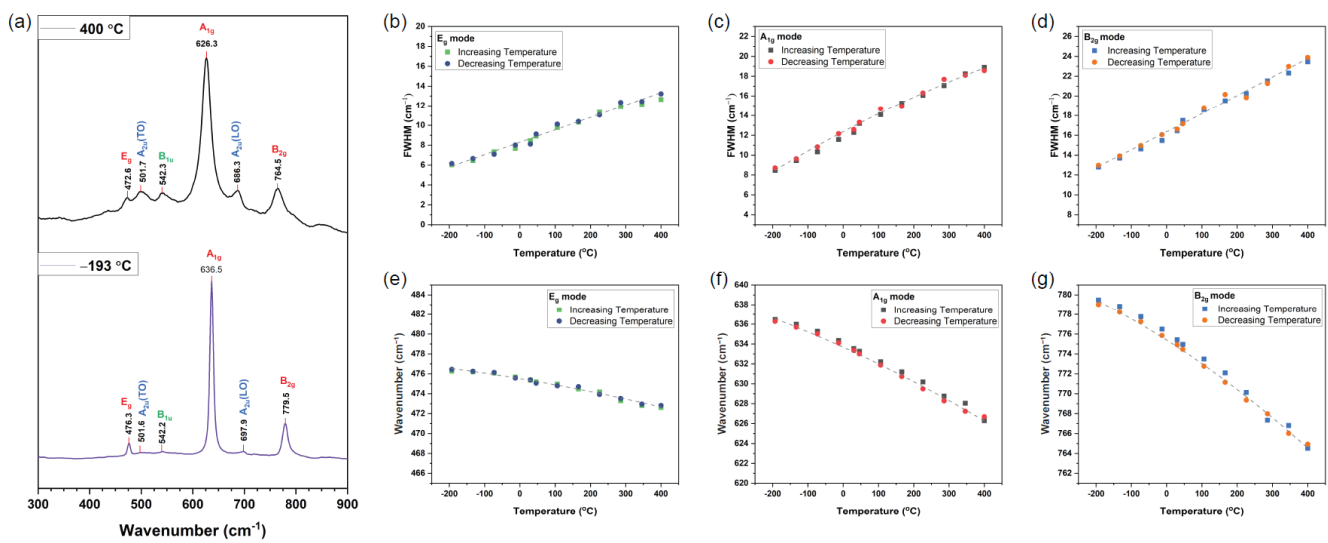
Figure 6. Spectra from powder samples were analyzed and interpreted to determine the presence of various vibrational modes. (**a**) The comparison of the two temperature extrema allows one to determine the extent of vibrational mode shifting. (**b**–**d**) The temperature dependence of the full width at half-maxima (FWHM) is shown for the E_g, A_{1g}, and B_{2g} modes, respectively. Datasets where temperature is being incrementally increased and decreased are both included to show a minimal contribution from hysteresis. (**e**–**g**) The temperature dependence of the peak center is shown for the E_g, A_{1g}, and B_{2g} modes.

At the Gamma point of the Brillouin zone for SnO_2, one expects various phonon responses, including: $1A_{1g} + 1B_{1g} + 1B_{2g} + 1E_g + 1A_{2g} + 2B_{1u} + 2A_{2u} + 4E_u$ [53]. The first four are Raman active, followed by two that are optically inactive, and concluded by two that are infrared (IR) active. Several additional modes appear in the data, especially with high temperatures (Figure 6a). One interpretation of these additional peaks involves forbidden modes that appear at high temperatures (greater than 300 °C) due to an increase in defect density or disorder in the material. It should be noted that IR modes can become weakly active when structural changes emerge due to a disorder.

Raman spectra from powder samples were analyzed and interpreted to determine the presence of various vibrational modes. For Figure 6b–d, the full widths at half-maxima (FWHM) are shown as a function of temperature for the E_g, A_{1g}, and B_{2g} modes, respectively. Datasets, where the temperature is incrementally increased and decreased, are both included to show a minimal contribution from hysteresis. The E_g mode exhibits a FWHM that only increases by about 7 cm^{-1} over the span of the temperature range, whereas the other two modes exhibit an increase of just over 10 cm^{-1}.

In Figure 6e–g, the peak centers are shown as a function of temperature for the E_g, A_{1g}, and B_{2g} modes, respectively. The peak centers were determined by Lorentzian fits to the Raman modes. It is evident from these plots that some of the modes experience stronger shifts than others, but all exhibit redshifting with increased temperature. The E_g, A_{1g}, and B_{2g} modes exhibit a redshift of about 3 cm^{-1}, 10 cm^{-1}, and 14 cm^{-1}, respectively. For the latter two modes, the trends appear to reflect a subtle nonlinear relationship with temperature, but the subtlety is great enough that fitting this behavior to a polynomial or other nonlinear function would have to be carried out arbitrarily until a greater range of temperatures could be measured.

Though the SnO_2 powder has provided us with ample information regarding the expected vibrational modes, it is still useful to obtain spectra of the various films to determine if there are any obvious signs of thickness dependence for those modes. As such, Figure 7 shows these data including the background spectrum for the bare quartz upon which the films reside. Raman spectra were collected for thicknesses of 908 nm, 373 nm, 97 nm, 78 nm, and 41 nm. Using the 908 nm film as an exemplary sample for the

non-powdered samples, several of the modes were assigned and are indicated in Figure 7b. It shows a peak pattern change between bare quartz and 908 nm SnO_2 film thickness. The bare quartz indicates a pronounced peak around 438 cm^{-1} due to Si-O-Si symmetric stretching [54,55]. Two peaks appeared at the 908 nm film at 238 cm^{-1} and 352 cm^{-1} that could be assigned to $E_U^{(1)}$(TO) and A_{2g} (optically inactive mode), respectively [56]. The peaks that are positioned at 487 cm^{-1} and 602 cm^{-1} in bare quartz and at 489 cm^{-1} and 604 cm^{-1} in the SnO_2 film are associated with D_1 and D_2 defect modes of 4-fold and 3-fold rings in the normal 6-fold rings of SnO_2 respectively 55, 57. The shoulder peak that appears on the SnO_2 film at 712 cm^{-1} can be assigned to $E_U^{(3)}$(LO) [56]. The 800 cm^{-1} peak that appears on bare quartz is associated with peak represented as ω_3 band that coincides with Si motion against the tetrahedral O cage as symmetric bond stretching (O-Si-O) [55–58]. The following peaks at 1055 cm^{-1} in bare quartz and 1064 cm^{-1} in SnO_2 film are associated with the symmetric stretching of Si-O [55].
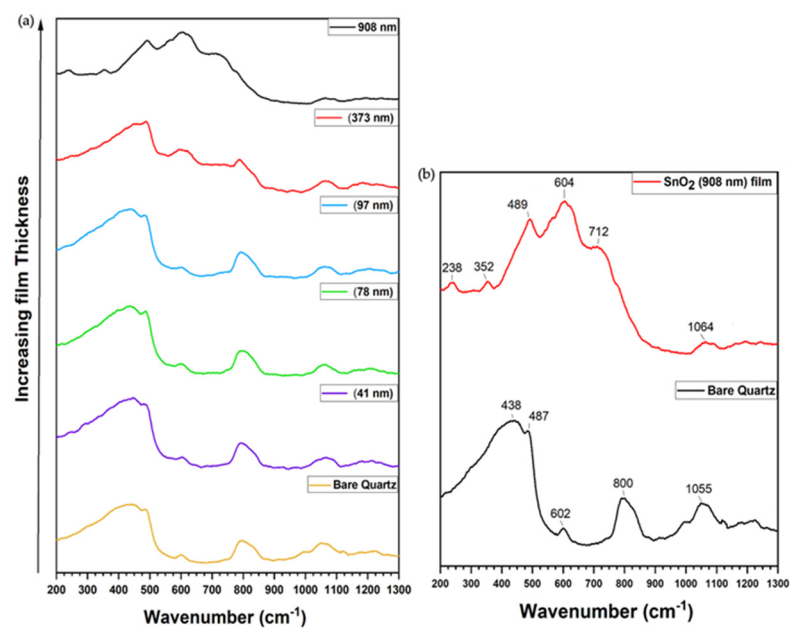

Figure 7. (**a**) Raman spectra are collected and shown from SnO_2 films of various thicknesses (908 nm, 373 nm, 97 nm, 78 nm, and 41 nm) as well as the bare quartz substrate. (**b**) Comparison between SnO_2 908 nm film thickness with bare quartz substrate at room temperature.

Since some of these modes also shift as a function of temperature, it was important to perform measurements with more granular steps. It should be noted that each of the three modes of interest are slightly shifted with respect to other work reported in the literature. For instance, in Bhadrapriya et al. [54], the E_g, A_{1g}, and B_{2g} modes are assigned at 476.6 cm^{-1}, 637.9 cm^{-1}, and 793.4 cm^{-1}, respectively. This aligns nicely with the powder samples, whose corresponding values (all at room temperature) are about 475 cm^{-1}, 634 cm^{-1}, and 775 cm^{-1}, respectively. However, that does not appear to be as true for the films. Using 908 nm, the assigned peaks take on values of about 490 cm^{-1}, 602 cm^{-1}, and 707 cm^{-1}, respectively. The reason for this shift may be attributed to factors such as contamination or oxygen vacancies in the SnO_2 samples. Additional data (to be presented in the next section) for both reasons must corroborate that attribution. Raman spectra generally do not show the band at around 582 cm^{-1} and A_{2u} band at around 694 cm^{-1}, indicating the lack of vacant sites and local lattice disorder as described in Gouvêa et al. and Kamali et al. [59,60].

Table 1 shows the different peak values associated with 908 nm film, bare quartz, and SnO_2 powder pellet and its effect with temperature. The majority of the SnO_2 film peaks are associated with SiO_2 (i.e., quartz glass) and can be summarized as follows:

1. It appeared that the 438 cm^{-1} Raman mode observed on bare quartz is close to the Zur et al. band of SiO$_2$-SnO$_2$ (transparent glass-ceramic) and could be assigned to vibrations of symmetric stretching of Si-O-Si bonds in six-membered rings which assigned to SiO$_4$ tetrahedra deformation vibration [55,57]. The narrowing of the 438 cm^{-1} peak is due to the existence of SnO$_2$ that could provoke a tighter Si-O-Si angle of SiO$_4$ tetrahedra or obstruct the construction of higher-membered rings [55,58]. Another study by McMillan associates the narrowing of the peak along with the wavenumber shift to the tighter Si-O-Si angle that is for a more compact SiO$_2$ structure. Therefore, adding SnO$_2$ to SiO$_2$ could have prevented the formation of higher-membered rings [61].

2. The two peaks at 488 cm^{-1} and 602 cm^{-1} in SnO$_2$ film and 487 cm^{-1} and 602 cm^{-1} in bare quartz are related to D$_1$ and D$_2$ defect bands that are assigned to the defects of 4-fold and 3-fold rings in the normal 6-fold rings of SnO$_2$, respectively [55,57]. It also appears that the addition of SnO$_2$ into the SiO$_2$ matrix has modified the 438 cm^{-1} peak with a D$_1$ defect band.

3. A shoulder peak of 602 cm^{-1} in the SnO$_2$ 908 nm film at room temperature and at −193 °C around 623 cm^{-1} could be related to the addition of SnO$_2$ to SiO$_2$. This band is weak and overlaps with the D$_1$ defect band due to the disorder of the SnO$_2$ nanoparticle [55,62]. The broadening of the A$_{1g}$ peak is due to a smaller grain size in the film.

4. The peak at 739 cm^{-1} is a shoulder peak of that at 783 cm^{-1}, which only appeared at −193 °C and may be due to E$_U^{(3)}$(LO). This value is closer to the specified value in Lan et al. [56].

5. Next, the 783 cm^{-1} peak is represented as a ω_3 band that coincides with the Si motion against the tetrahedral O cage as symmetric bond stretching (O-Si-O) [55–58].

6. Finally, the peak that appears on SnO$_2$ film at 1063 cm^{-1} and on bare quartz at 1055 cm^{-1} is associated with the symmetric stretching of Si-O [55].

Table 1. Comparison of vibrational modes observed for SnO$_2$ 908 nm film, bare quartz, and SnO$_2$ powder [55].

Modes (All Units cm^{-1})	908 nm Film		Bare Quartz	Zur et al. [55]	Modes	SnO$_2$ Powder	
Ambient Condition	**−193 °C**	**400 °C**		**30 °C**		**−193 °C**	**400 °C**
Si-O-Si (symmetric stretching)	—		438	440	—	—	
D$_1$ defect bands	488	460	487	489	E$_g$	476	472
—	—		—	—	A$_{2u}$(TO)	501	
—	—		—	—	B$_{1u}$	542	
D$_2$ defect bands	602	606	602	600	A$_{1g}$	636	626
—	—		—	—	A$_{2u}$(LO)	697	686
—	739	—	—	—	—	—	
O-Si-O (symmetric stretching)	783		800	800	B$_{2g}$	779	764
Si-O (symmetric stretching)	1063	1050	1055	—	—	—	

Again, the 908 nm film was used as an example in determining the temperature dependence of various Raman modes. All of these spectra are shown in Figure 8, with the same plotting scheme adopted from Figure 7, where both increasing and decreasing temperature data are shown. All experimental parameters are listed in the Methods section. In Figure 8a (left panel), several of the modes are tracked with dashed vertical lines, with the former panel conducted in a similar fashion to the powder samples. However, for Figure 8a (right panel), dashed lines are drawn to highlight the shifts observed in the three modes with temperature as a guide for the eye. All of the peaks consistently redshift with increasing temperature, as seen in the powder samples. The extent of shifting is

even of similar value, but it is more difficult to conclude a similarity in trends with the FWHM because the peaks have a characteristically larger error when being fit with a Lorentzian profile.
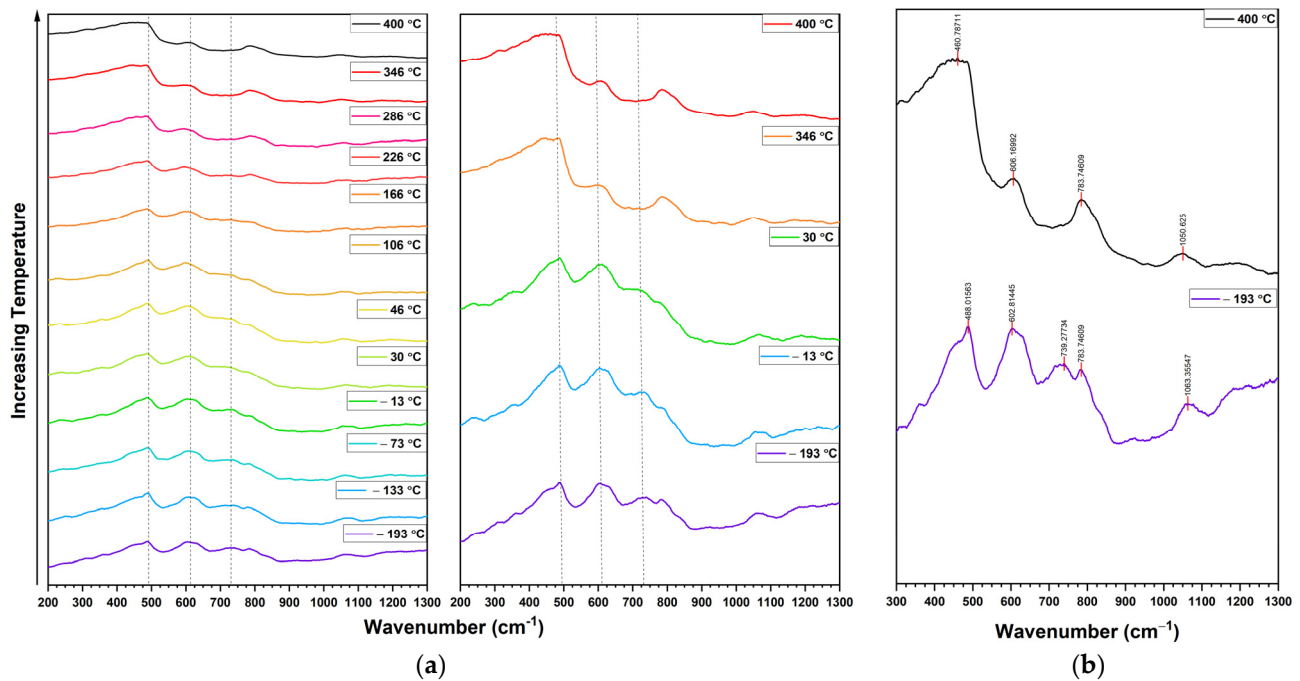
Figure 8. Samples with a 908 nm thick SnO$_2$ film were measured at experimental parameters listed in the Methods section. (**a**) A series of Raman spectra are shown as a function of temperature, starting with −193 °C and ending with 400 °C with sample of five spectra were plotted with greater vertical scaling to distinguish the changes apparent with some of the vibrational modes. (**b**) In the case of the 908 nm-thick film, the two temperature extrema (400 °C and −193 °C in black and purple, respectively) are shown with demarcations of various modes' peak positions.

2.3. X-ray Photoelectron Spectroscopy

X-ray photoelectron spectroscopy helps one determine if any impurities get introduced during the synthesis of the films and powders. Furthermore, the technique helps one verify the stoichiometric ratio and general composition of all of the materials. Figures 9 and 10 show an array of data obtained for each film thickness and the powder form. More specifically, Figure 9 shows the survey scans, the oxygen 1s electrons, and the tin 3d electrons, whereas Figure 10 shows the nitrogen 1s electrons, carbon 1s electrons, and silicon 2p electrons.

The survey scans show mostly standard behavior with the one exception that there may be indium contamination, as exemplified by the subtle peaks at about 460 eV (one of the sputter targets had a minuscule amount of indium as well). This observation corroborates the aforementioned suspicion on the possibility of dopants modifying observed Raman modes. As far as the oxygen scan goes, one interesting observation to point out is the presence and trending behavior of the non-oxide peak near 532 eV. Not only does powdered SnO$_2$ show the most subdued non-oxide peak, but the contribution itself increases for the film samples (though it does not have a strong thickness dependence). Despite not linearly increasing in contribution, the non-oxide peak does, in fact, shift to slightly higher binding energies with increasing thickness. For the third column of data, focused on the tin 3d electrons, no reliable trends are observable, with the exception of a generally increased energy for the relevant electrons observed in the 41 nm film and the powder samples.
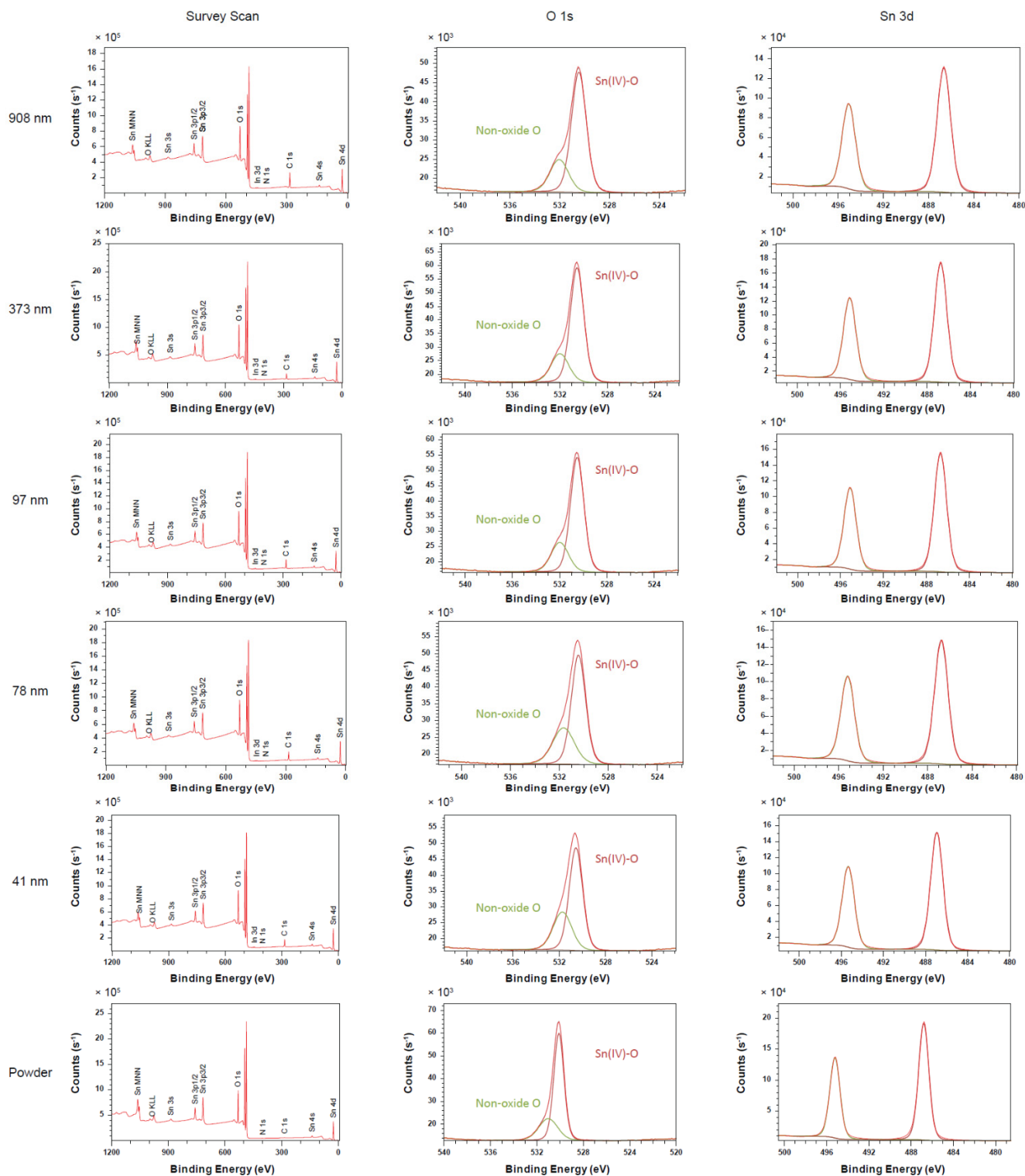
Figure 9. Many XPS measurements are shown in descending order of thickness, concluded by the powder samples. Each column is designated as one for either a survey scan, O 1s electrons, or Sn 3d electrons.
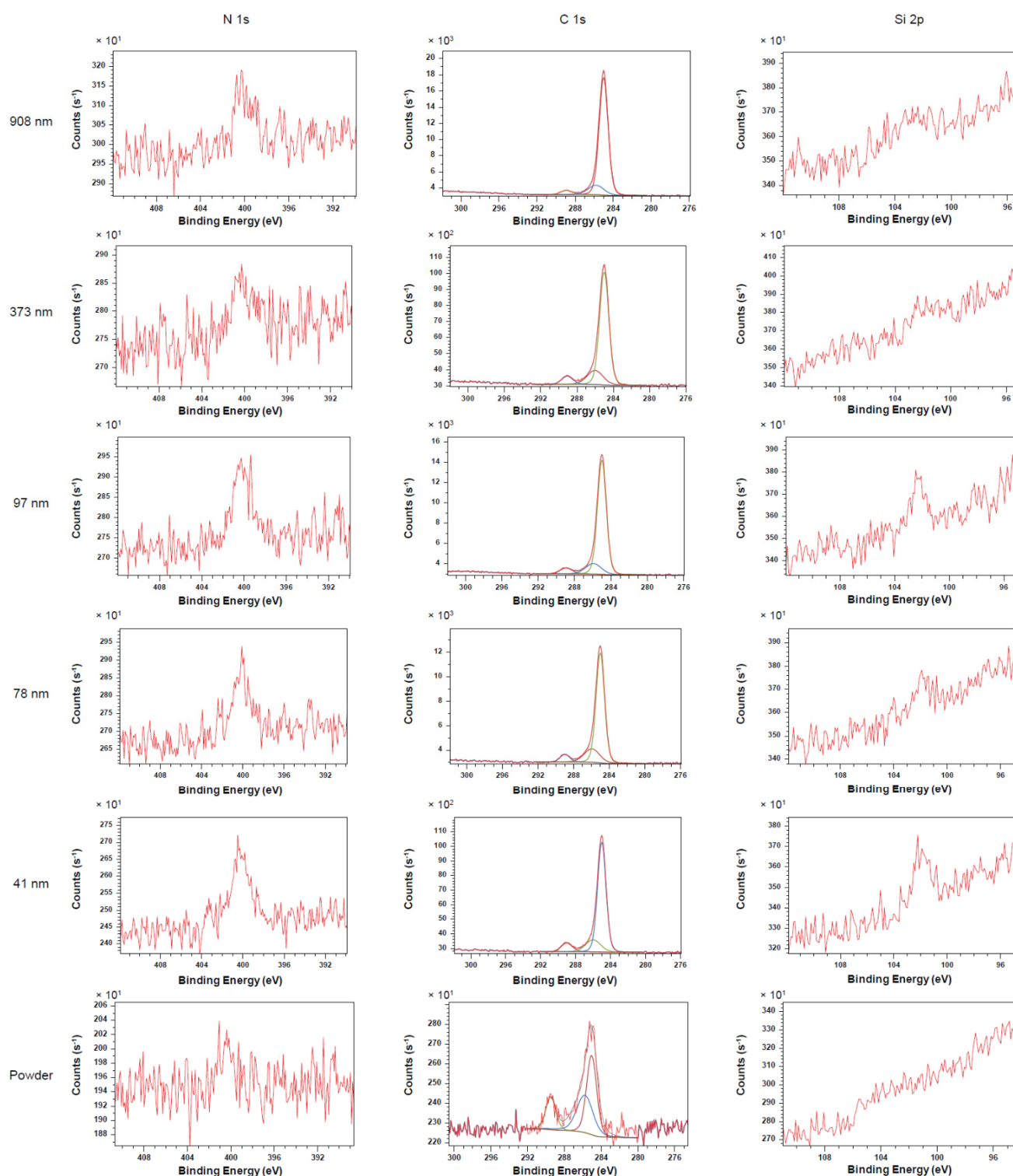
Figure 10. Many XPS measurements are shown in descending order of thickness, concluded by the powder samples. Each column is designated as one for either N 1s electrons, C 1s electrons, or Si 2p electrons. Minimal Si counts relative to other electrons suggests adequate enough coverage of films on quartz substrates such that substrate is not probed.

Additional observations can be noted from the data shown in Figure 8, starting with the nitrogen 1s electrons. The difference seen is mainly between film and powder, where the response from the powder is 4 to 5 times lower than its film counterpart. Lastly, the silicon 2p electrons exhibit the smallest of all the responses, with none recorded from the

powder, and very weak signals recorded from the films. No strong measurable trend can be extracted from the data collected on the samples. All experimental parameters are described in the Methods section.

The XPS peak positions were extracted by fitting them with Lorentzian profiles, with the relevant data presented in Tables 2 and 3. One observation that remains interesting is that the non-oxide oxygen 1s electrons appear to demonstrate a response that shifts with the film thickness, as also mentioned earlier by reviewing the plots in Figure 9. Though the shifting is very gradual, it does fall within the range of uncertainties from the fitting procedure. A closer look at the elemental percentages from Figure 9 reveals that, although Sn percentages are uncorrelated with thickness, the non-oxide oxygen composition is weighted slightly more heavily for thinner samples, within the errors of the fitting procedures. A thickness of about 100 nm appears to divide the elemental composition by a few percent.

Table 2. Tabulated sample peak positions are determined with Lorentzian profile fitting. The positions are averaged within the relevant set of data and accompanied by a 1σ error from the peak fitting procedures.

Sample Peak Positions (Averaged, with 1σ Error from Peak Fitting)				
Sample Type	Sn 3d 5/2	Sn 3d 3/2	O 1s (Oxide)	O 1s (Non-Oxide)
908 nm	486.65 ± 0.02	495.07 ± 0.02	530.48 ± 0.03	532.05 ± 0.02
373 nm	486. 74 ± 0.02	495.16 ± 0.02	530.57 ± 0.03	532.03 ± 0.05
97 nm	486.71 ± 0.01	495.12 ± 0.01	530.52 ± 0.02	531.98 ± 0.03
78 nm	486.80 ± 0.04	495.21 ± 0.04	530.48 ± 0.04	531.73 ± 0.06
41 nm	486.90 ± 0.03	495.31 ± 0.03	530.53 ± 0.03	531.66 ± 0.08
Powder	486.81 ± 0.13	495.23 ± 0.14	530.49 ± 0.36	531.40 ± 0.35

Table 3. Tabulated composition percentages from XPS spectra of various forms of SnO_2.

Sample Elemental Percentages (Averaged, with 1σ Error from Peak Fitting)				
Sample Type	Sn %	Oxide O %	Non-Oxide O %	Total O %
908 nm	37.75 ± 0.25	46.43 ± 0.41	15.81 ± 0.66	62.24 ± 0.26
373 nm	38.31 ± 0.19	46.62 ± 0.50	15.02 ± 0.39	61.69 ± 0.19
97 nm	37.79 ± 0.41	46.03 ± 1.29	16.19 ± 1.69	62.21 ± 0.41
78 nm	38.27 ± 0.15	42.17 ± 0.87	19.55 ± 1.02	61.73 ± 0.15
41 nm	37.83 ± 0.02	40.44 ± 1.16	21.73 ± 1.18	62.17 ± 0.02
Powder	40.06 ± 0.20	43.44 ± 0.24	16.49 ± 0.12	59.93 ± 0.20

3. Methods

Methods are generally summarized in Figure 11. The SnO_2 powder was acquired from SIGMA-ALDRICH.[∂] It has 99.9% purity with 325 mesh, with a target being six-inch diameter high purity 99.99% ceramic SnO_2 with a small percentage (0.5%) of indium. It was annealed at 1000 °C for 1 hour. SnO_2 thin samples on 0.1-inch quartz thick were provided by General Monitors and manufactured by radio frequency (RF) sputter deposition in an oxygen/argon mixed atmosphere. The sputter times varied on the single-digit minute scale. [∂] The deposited SnO_2 film thickness was monitored by sputter deposition onto a polished silicon substrate [63]. Double-sided polished silicon was used to enable infrared transmission measurement studies and visible-ultraviolet reflectance measurements that were used to calculate the SnO_2 film thickness. A Filmetrics F20 instrument was used for curve fitting to calculate film thickness. [∂] Film thickness was varied by changing the sputter

deposition time. UV–quartz substrates were placed in the sputtering machine alongside the polished silicon thickness monitor substrate [64].

SEM	AFM	Raman	XPS
• SnO$_2$ powder SnO$_2$ films on quartz: • 41 nm • 78 nm • 97 nm • 373 nm • 908 nm	• SnO$_2$ powder SnO$_2$ films on quartz: • 373 nm • 908 nm	• SnO$_2$ powder SnO$_2$ films on quartz: • 908 nm	• SnO$_2$ powder SnO$_2$ films on quartz: • 41 nm • 78 nm • 97 nm • 373 nm • 908 nm

Figure 11. Summary of all samples and corresponding tests carried out in this paper.

SEM data were acquired with a FEI Helios Focused Ion Beam,[∂] with a magnification that ranged from 200× to 200,000×. Other parameters are as follows: 2 kV, 0.1 nA, 746 nm horizontal field width, 10 µs dwell time, use of through lens detector, 0° tilt, and a 3.8 mm working distance. The samples were placed on a holder and then loaded into a chamber where plasma cleaning was applied to clean carbon from the sample surfaces. The images were obtained with the Everhart–Thornley detector (TLD) mode for better resolution, especially for the film samples. The SnO$_2$ powder was sprinkled lightly on carbon tape, whereas the SnO$_2$ films on quartz were placed on carbon tape and atop copper tape for better conductivity and resolution. The cross-section images were collected by using Phenom Pure Desktop SEM (Nanoscience Instrument) operated at a magnification that ranges between 20× to 65,000×. The EDS analysis was obtained using JEOL JSM-7100F SEM with magnification ranges from 10× to 500,000×.

The Atomic Force Microscope (AFM) images were recorded by using The Bruker Dimension FastScan atomic force microscope (AFM) combines a high-speed scanning AFM and programmable stage control. It provides rapid nanoscale imaging capabilities on substrates ranging from 200 mm diameter wafers down to small pieces. The system supports scan areas of up to 35 µm × 35 µm and can automatically collect data from multiple locations on a substrate.

Raman spectroscopy data were recorded on a Renishaw via Raman spectrometer using a 514 nm wavelength excitation laser source, laser beam quality of 0.65 mm, and laser maximum power of 50 mW.[∂] The spectra were collected using a laser exposure time of 10 s, 50× objective, and 3 accumulations to reduce the signal-to-noise ratio. The Linkam LTS420 heating and freezing stage and T96 LinkPad system controller with a maximum heating rate of 40 °C/min were used with Raman spectroscopy. The maximum stage temperature was 420 °C, and the minimum temperature was −195 °C with a LNP96-S liquid nitrogen cooling pump. To prevent condensation on the stage window surface during cooling, two steps were carried out: (1) a small tube was placed on the stage window that blows warm recycled nitrogen, and (2) air was purged from the stage chamber with dry nitrogen.

XPS measurements were performed using the Kratos Axis Ultra X-ray photoelectron spectrometer operating at a base pressure of about 2.66×10^{-7} Pa (about 2×10^{-9} Torr).[∂] All samples were analyzed using monochromatic Al K$_\alpha$ (1486.7 eV) with spot size 300 µm × 700 µm. Pass energies of 160 eV and 20 eV were used to collect the survey and high-resolution core level XPS spectra, respectively. All experimental uncertainties (1σ) arise from the uncertainty of the instrumentation used for this work.

$^{\partial}$ **Commercial equipment:** Instruments and materials are identified in this paper in order to specify the experimental procedure adequately. Such identification is not intended to imply recommendation or endorsement by the National Institute of Standards and Technology or the United States government, nor is it intended to imply that the materials or equipment identified are necessarily the best available for the purpose.

[#] **Though not an SI Unit:** This unit is permitted for expressing data by the International Committee for Weights and Measures (CIPM) and the National Institute of Standards and Technology.

References

1. Lee, I.; Choi, S.-J.; Park, K.-M.; Lee, S.S.; Choi, S.; Kim, I.-D.; Park, C.O. The stability, sensitivity and response transients of ZnO, SnO_2 and WO_3 sensors under acetone, toluene and H2S environments. *Sens. Actuators B Chem.* **2014**, *197*, 300–307. [CrossRef]
2. Yuliarto, B.; Gumilar, G.; Septiani, N.L.W. SnO_2 nanostructure as pollutant gas sensors: Synthesis, sensing performances, and mechanism. *Adv. Mater. Sci. Eng.* **2015**, *2015*, 694823. [CrossRef]
3. Sharma, A.; Tomar, M.; Gupta, V. SnO2 thin film sensor with enhanced response for NO_2 gas at lower temperatures. *Sens. Actuators B Chem.* **2011**, *156*, 743–752. [CrossRef]
4. Gong, J.; Chen, Q.; Lian, M.-R.; Liu, N.-C.; Stevenson, R.G.; Adami, F. Micromachined nanocrystalline silver doped SnO_2 H_2S sensor. *Sens. Actuators B Chem.* **2006**, *114*, 32–39. [CrossRef]
5. Korotcenkov, G.; Brinzari, V.; Cho, B.K. In_2O_3-and SnO_2-based thin film ozone sensors: Fundamentals. *J. Sens.* **2016**, *2016*, 1–32. [CrossRef]
6. Suman, P.H.; Felix, A.A.; Tuller, H.L.; Varela, J.A.; Orlandi, M.O. Comparative gas sensor response of SnO_2, SnO and Sn_3O_4 nanobelts to NO_2 and potential interferents. *Sens. Actuators B Chem.* **2015**, *208*, 122–127. [CrossRef]
7. Mills, S.; Lim, M.; Lee, B.; Misra, V. Atomic layer deposition of SnO_2 for selective room temperature low ppb level O_3 sensing. *ECS J. Solid State Sci. Technol.* **2015**, *4*, S3059. [CrossRef]
8. Kim, B.; Lu, Y.; Hannon, A.; Meyyappan, M.; Li, J. Low temperature Pd/SnO_2 sensor for carbon monoxide detection. *Sens. Actuators B Chem.* **2013**, *177*, 770–775. [CrossRef]
9. Vishwakarma, S.R.; Prasad, H.C. Low cost SnO_2: $P/SiO_2/n$-Si (textured) heterojunction solar cells. *J. Phys. D Appl. Phys.* **1993**, *26*, 959. [CrossRef]
10. Vasu, V.; Subrahmanyam, A. Photovoltaic properties of indium tin oxide (ITO)/silicon junctions prepared by spray pyrolysis-dependence on oxidation time. *Semiconductor Sci. Technol.* **1992**, *7*, 320. [CrossRef]
11. Ferlauto, A.S.; Ferreira, G.M.; Pearce, J.M.; Wronski, C.R.; Collins, R.W.; Deng, X.; Ganguly, G. Analytical model for the optical functions of amorphous semiconductors from the near-infrared to ultraviolet: Applications in thin film photovoltaics. *J. Appl. Phys.* **2002**, *92*, 2424–2436. [CrossRef]

12. Tennakone, K.; Kumara, G.R.R.A.; Kottegoda, I.R.M.; Perera, V.P.S. An efficient dye-sensitized photoelectrochemical solar cell made from oxides of tin and zinc. *Chem. Commun.* **1999**, 15–16. [CrossRef]

13. Zheng, J.P.; Kwok, H.S. Preparation of indium tin oxide films at room temperature by pulsed laser deposition. *Thin Solid Films* **1993**, *232*, 99–104. [CrossRef]

14. Ito, S.; Makari, Y.; Kitamura, T.; Wada, Y.; Yanagida, S. Fabrication and characterization of mesoporous SnO_2/ZnO-composite electrodes for efficient dye solar cells. *J. Mater. Chem.* **2004**, *14*, 385–390. [CrossRef]

15. Bagheri-Mohagheghi, M.M.; Shokooh-Saremi, M. The influence of Al doping on the electrical, optical and structural properties of SnO_2 transparent conducting films deposited by the spray pyrolysis technique. *J. Phys. D Appl. Phys.* **2004**, *37*, 1248. [CrossRef]

16. Liu, C.; Matsutani, T.; Yamamoto, N.; Kiuchi, M. High-quality indium tin oxide films prepared at room temperature by oxygen ion beam assisted deposition. *EPL Europhys. Lett.* **2002**, *59*, 606–611. [CrossRef]

17. Reddy, V.S.; Das, K.; Dhar, A.; Ray, S.K. The effect of substrate temperature on the properties of ITO thin films for OLED applications. *Semicond. Sci. Technol.* **2006**, *21*, 1747–1752. [CrossRef]

18. LavrenčičáŠtangar, U. Preparation and characterization of Mo-and Sb: Mo-doped SnO_2 sol-gel-derived films for counter-electrode applications in electrochromic devices. *J. Mater. Chem.* **1995**, *5*, 617–624.

19. Kityk, I.V.; Eboth, J.; Miedzinski, R.; Addou, M.; Sieder, H.; Karafiat, A. Optically-induced non-linear optical effects in indium–tin oxide crystalline films. *Semicond. Sci. Technol.* **2003**, *18*, 549–553. [CrossRef]

20. Morgado, J.; Barbagallo, N.; Charas, A.; Matos, M.; Alcácer, L.; Cacialli, F. Self-assembly surface modified indium-tin oxide anodes for single-layer light-emitting diodes. *J. Phys. D Appl. Phys.* **2003**, *36*, 434–438. [CrossRef]

21. Suzuki, T.; Yamazaki, T.; Oda, H. Effects of composition and thickness on the electrical properties of indium oxide/tin oxide multilayered films. *J. Mater. Sci.* **1989**, *24*, 1383. [CrossRef]

22. Guillén, C.; Herrero, J. Influence of the film thickness on the structure, optical and electrical properties of ITO coatings deposited by sputtering at room temperature on glass and plastic substrates. *Semicond. Sci. Technol.* **2008**, *23*, 075002. [CrossRef]

23. Munir, M.M.; Iskandar, F.; Yun, K.M.; Okuyama, K.; Abdullah, M. Optical and electrical properties of indium tin oxide nanofibers prepared by electrospinning. *Nanotechnology* **2008**, *19*, 145603. [CrossRef] [PubMed]

24. Ferrere, S.; Zaban, A.; Gregg, B.A. Dye sensitization of nanocrystalline tin oxide by perylene derivatives. *J. Phys. Chem. B* **1997**, *101*, 4490–4493. [CrossRef]

25. Huang, H.; Tan, O.K.; Lee, Y.C.; Tran, T.D.; Tse, M.S.; Yao, X. Semiconductor gas sensor based on tin oxide nanorods prepared by plasma-enhanced chemical vapor deposition with post plasma treatment. *Appl. Phys. Lett.* **2005**, *87*, 163123. [CrossRef]

26. Varghese, O.K.; Malhotra, L.K. Electrode-sample capacitance effect on ethanol sensitivity of nano-grained SnO_2 thin films. *Sens. Actuators B Chem.* **1998**, *53*, 19–23. [CrossRef]

27. Sakanoue, T.; Nakatani, S.; Ueda, Y.; Izumi, H.; Ishihara, T.; Motoyama, M. Fabrication of well-ordered indium-tin-oxide film and characterization of organic films vacuum-deposited on it. *Mol. Cryst. Liq. Cryst.* **2003**, *405*, 59–66. [CrossRef]

28. Khanna, A.; Kumar, R.; Bhatti, S.S. CuO doped SnO_2 thin films as hydrogen sulfide gas sensor. *Appl. Phys. Lett.* **2003**, *82*, 4388. [CrossRef]

29. Comini, E.; Faglia, G.; Sberveglieri, G.; Pan, Z.; Wang, Z.L. Stable and highly sensitive gas sensors based on semiconducting oxide nanobelts. *Appl. Phys. Lett.* **2002**, *81*, 1869–1871. [CrossRef]

30. Song, J.E.; Lee, D.K.; Kim, Y.H.; Kang, Y.S. Preparation of water dispersed indium tin oxide sol solution. *Mol. Cryst. Liq. Cryst.* **2006**, *444*, 247–255. [CrossRef]

31. Coles, G.S.V.; Williams, G.; Smith, B.J. The effect of oxygen partial pressure on the response of tin (IV) oxide based gas sensors. *J. Phys. D Appl. Phys.* **1991**, *24*, 633–641. [CrossRef]

32. Panchapakesan, B.; DeVoe, D.L.; Widmaier, M.R.; Cavicchi, R.; Semancik, S. Nanoparticle engineering and control of tin oxide microstructures for chemical microsensor applications. *Nanotechnology* **2001**, *12*, 336–349. [CrossRef]

33. Choi, Y.J.; Hwang, I.-S.; Park, J.-G.; Choi, K.J.; Park, J.H.; Lee, J.-H. Novel fabrication of an SnO_2 nanowire gas sensor with high sensitivity. *Nanotechnology* **2008**, *19*, 095508. [CrossRef]

34. Eastwood, P.G.; Claypole, T.C.; Watson, J.; Coles, G.S.V. The behaviour of tin dioxide sensors in exhaust environments at low and intermediate temperatures. *Meas. Sci. Technol.* **1993**, *4*, 524–533. [CrossRef]

35. Llobet, E.; Vilanova, X.; Brezmes, J.; Alcubilla, R.; Calderer, J.; Sueiras, J.E.; Corrie, X. Conductance-transient analysis of thick-film tin oxide gas sensors under successive gas-injection steps. *Meas. Sci. Technol.* **1997**, *8*, 1133–1138. [CrossRef]

36. Partridge, J.G.; Field, M.R.; Peng, J.L.; Sadek, A.Z.; Kalantar-zadeh, K.; Du Plessis, J.; McCulloch, D.G. Nanostructured SnO_2 films prepared from evaporated Sn and their application as gas sensors. *Nanotechnology* **2008**, *19*, 125504. [CrossRef]

37. Colomban, P.; Gironda, M.; Franci, G.S.; d'Abrigeon, P. Distinguishing Genuine Imperial Qing Dynasty Porcelain from Ancient Replicas by On-Site Non-Invasive XRF and Raman Spectroscopy. *Materials* **2022**, *15*, 5747. [CrossRef]

38. Alamrani, F.; Alsharaeh, E. Controlling the Bandgaps of One-Dimensional TiO_2/SiO_2, TiO_2/SnO_2, and SiO_2/SnO_2 Photonic Crystals Using the Transfer Matrix Method. *Optics Photon. J.* **2022**, *12*, 171–189. [CrossRef]

39. Gotschy, W.; Vonmetz, K.; Leitner, A.; Aussenegg, F.R. Thin films by regular patterns of metal nanoparticles: Tailoring the optical properties by nanodesign. *Appl. Phys. B* **1996**, *63*, 381–384. [CrossRef]

40. Dhatarwal, P.; Sengwa, R.J.; Choudhary, S. Multifunctional (PVP/PEO)/SnO_2 nanocomposites of tunable optical and dielectric properties. *Optik* **2020**, *221*, 165368. [CrossRef]

41. Kavan, L. Conduction band engineering in semiconducting oxides (TiO$_2$, SnO$_2$): Applications in perovskite photovoltaics and beyond. *Catal. Today* **2019**, *328*, 50–56. [CrossRef]
42. Subbiah, A.S.; Mathews, N.; Mhaisalkar, S.G.; Sarkar, S.K. Novel Plasma-assisted low-temperature-processed SnO$_2$ thin films for efficient flexible perovskite photovoltaics. *ACS Energy Lett.* **2018**, *3*, 1482–1491. [CrossRef]
43. Dalapati, G.K.; Sharma, H.; Guchhait, A.; Chakrabarty, N.; Bamola, P.; Liu, Q.; Saianand, G.; Krishna, A.M.S.; Mukhopadhyay, S.; Dey, A.; et al. Tin oxide for optoelectronic, photovoltaic and energy storage devices: A review. *J. Mater. Chem. A* **2021**, *9*, 16621–16684. [CrossRef]
44. Yu, H.; Yeom, H.-I.; Lee, J.W.; Lee, K.; Hwang, D.; Yun, J.; Ryu, J.; Lee, J.; Bae, S.; Kim, S.K.; et al. Superfast room-temperature activation of SnO$_2$ thin films via atmospheric plasma oxidation and their application in planar perovskite photovoltaics. *Adv. Mater.* **2018**, *30*, 1704825. [CrossRef]
45. Pyke, D.R.; Reid, R.; Tilley, R.J.D. Structures of tin oxide—antimony oxide catalysts. *J. Chem. Soc. Faraday Trans. 1 Phys. Chem. Condens. Phases* **1980**, *76*, 1174–1182. [CrossRef]
46. Dodd, A.; McKinley, A.; Saunders, M.; Tsuzuki, T. Mechanochemical synthesis of nanocrystalline SnO$_2$–ZnO photocatalysts. *Nanotechnology* **2006**, *17*, 692. [CrossRef]
47. Cai, X.; Ogorevc, B.; Tavčar, G.; Wang, J. Indium—Tin oxide film electrode as catalytic amperometric sensor for hydrogen peroxide. *Analyst* **1995**, *120*, 2579–2583. [CrossRef]
48. Jyothi, T.M.; Sugunan, S.; Rao, B.S. Selective methylation of anisole to 2,6-xylenol over rare earth promoted SnO$_2$ catalysts. *Green Chem.* **2000**, *2*, 269–271. [CrossRef]
49. Bond, G.C.; Molloy, L.R.; Fuller, M.J. Oxidation of carbon monoxide over palladium—tin(IV) oxide catalysts: An example of spillover catalysis. *J. Chem. Soc. Chem. Commun.* **1975**, 796–797. [CrossRef]
50. Hines, R.I.; Allan, N.L.; Flavell, W.R. Oxidation catalysts: A comparative simulation study of the lattice, defect and surface structure of the stannates ASnO$_3$(A = Ca, Sr and Ba) and SnO$_2$. *J. Chem. Soc. Faraday Trans.* **1996**, *92*, 2057–2063. [CrossRef]
51. He, Z.-K.; Sun, Q.; Xie, K.; Lu, P.; Shi, Z.; Kamali, A.R. Reactive molten salt synthesis of natural graphite flakes decorated with SnO2 nanorods as high performance, low cost anode material for lithium ion batteries. *J. Alloy. Compd.* **2019**, *792*, 1213–1222. [CrossRef]
52. Kohl, D.; Thoren, W.; Schnakenberg, U.; Schüll, G.; Heiland, G. Decomposition of gaseous acetic acid on SnO$_2$. *J. Chem. Soc. Faraday Trans.* **1991**, *87*, 2647–2653. [CrossRef]
53. Bonu, V.; Das, A.; Sivadasan, A.K.; Tyagi, A.K.; Dhara, S. Invoking forbidden modes in SnO$_2$ nanoparticles using tip enhanced Raman spectroscopy. *J. Raman Spectrosc.* **2015**, *46*, 1037–1040. [CrossRef]
54. Bhadrapriya, B.C.; Varghese, A.R.; Amarendra, G.; Hussain, S. Sb:SnO$_2$ thin films—Synthesis and characterization. *AIP Conf. Proc.* **2018**, *1951*, 030006.
55. Zur, L.; Tran, L.T.N.; Massella, D.; Vaccari, A.; Chiappini, A.; Chiasera, A.; Varas, S.; Armellini, C.; Carpentiero, A.; Boulard, B.; et al. SiO$_2$-SnO$_2$ transparent glass-ceramics activated by rare earth ions. *Opt. Compon. Mater.* **2019**, *10914*, 180–188.
56. Lan, T.; Li, C.W.; Fultz, B. Phonon anharmonicity of rutile SnO$_2$ studied by Raman spectrometry and first principles calculations of the kinematics of phonon-phonon interactions. *Phys. Rev. B* **2012**, *86*, 134302. [CrossRef]
57. Manghnani, M.H.; Hushur, A.; Sekine, T.; Wu, J.; Stebbins, J.F.; Williams, Q. Raman, Brillouin, and nuclear magnetic resonance spectroscopic studies on shocked borosilicate glass. *J. Appl. Phys.* **2011**, *109*, 113509. [CrossRef]
58. Van Tran, T.; Turrell, S.; Eddafi, M.; Capoen, B.; Bouazaoui, M.; Roussel, P.; Berneschi, S.; Righini, G.C.; Ferrari, M.; Bhaktha, S.N.B.; et al. Investigations of the effects of the growth of SnO$_2$ nanoparticles on the structural properties of glass–ceramic planar waveguides using Raman and FTIR spectroscopies. *J. Mol. Struct.* **2010**, *976*, 314–319. [CrossRef]
59. Gouvêa, D.; Pereira, G.J.; Gengembre, L.; Steil, M.C.; Roussel, P.; Rubbens, A.; Hidalgo, P.; Castro, R.H. Quantification of MgO surface excess on the SnO$_2$ nanoparticles and relationship with nanostability and growth. *Appl. Surf. Sci.* **2011**, *257*, 4219–4226. [CrossRef]
60. Kamali, A.R.; Fray, D.J. Solid phase growth of tin oxide nanostructures. *Mater. Sci. Eng. B* **2012**, *177*, 819–825. [CrossRef]
61. McMillan, P.F.; Remmele, R.L. Hydroxyl sites in SiO$_2$ glass: A note on infrared and Raman spectra. *Am. Mineral.* **1986**, *71*, 772–778.
62. Van Tran, T.T.; Bui, T.S.; Turrell, S.; Capoen, B.; Roussel, P.; Bouazaoui, M.; Ferrari, M.; Cristini, O.; Kinowski, C. Controlled SnO$_2$ nanocrystal growth in SiO$_2$-SnO$_2$ glass-ceramic monoliths. *J. Raman Spectrosc.* **2012**, *43*, 869–875. [CrossRef]
63. Saji, K.J.; Mary, A.P.R. Tin oxide based p and n-type thin film transistors developed by RF sputtering. *ECS J. Solid State Sci. Technol.* **2015**, *4*, Q101–Q104. [CrossRef]
64. Alghamdi, H.; Concepcion, B.; Baliga, S.; Misra, P. Synthesis, spectroscopic characterization and applications of tin dioxide. In *Contemporary Nanomaterials in Material Engineering Applications*; Springer: Cham, Switzerland, 2021; pp. 285–318.